NEOPLASIA
www.neoplasia.com

Volume 18 Number 12 December 2016 pp. 742–752 742

# Multimodality Imaging Identifies Distinct Metabolic Profiles *In Vitro* and *In Vivo*[1]

**Marie-Aline Neveu*, Géraldine De Preter*, Valérie Marchand*, Anne Bol†, Jeffery R. Brender‡, Keita Saito‡, Shun Kishimoto‡, Paolo E. Porporato§, Pierre Sonveaux§, Vincent Grégoire†, Olivier Feron§, Bénédicte F. Jordan*, Murali C. Krishna‡ and Bernard Gallez***

*Biomedical Magnetic Resonance Research Group, Louvain Drug Research Institute (LDRI), Université catholique de Louvain, Brussels, Belgium; †Radiation Oncology Department & Center for Molecular Imaging, Radiotherapy & Oncology, Institute of Experimental and Clinical Research (IREC), Université catholique de Louvain, Brussels, Belgium; ‡Radiation Biology Branch, National Cancer Institute, NIH, Bethesda, USA; §Pole of Pharmacology and Therapeutics, Institute of Experimental and Clinical Research (IREC), Université catholique de Louvain, Brussels, Belgium

## Abstract

The study of alterations of tumor metabolism should allow the identification of new targets for innovative anticancer strategies. Metabolic alterations are generally established *in vitro*, and conclusions are often extrapolated to the *in vivo* situation without further tumor metabolic phenotyping. To highlight the key role of microenvironment on tumor metabolism, we studied the response of glycolytic and oxidative tumor models to metabolic modulations *in vitro* and *in vivo*. MDA-MB-231 and SiHa tumor models, characterized *in vitro* as glycolytic and oxidative, respectively, were studied. Theoretically, when passing from a hypoxic state to an oxygenated state, a Warburg phenotype should conserve a glycolytic metabolism, whereas an oxidative phenotype should switch from glycolytic to oxidative metabolism (Pasteur effect). This challenge was applied *in vitro* and *in vivo* to evaluate the impact of different oxic conditions on glucose metabolism. $^{18}$F-fluorodeoxyglucose uptake, lactate production, tumor oxygenation, and metabolic fluxes were monitored *in vivo* using positron emission tomography, microdialysis, electron paramagnetic resonance imaging, and $^{13}$C-hyperpolarizated magnetic resonance spectroscopy, respectively. *In vitro*, MDA-MB-231 cells were glycolytic under both hypoxic and oxygenated conditions, whereas SiHa cells underwent a metabolic shift after reoxygenation. On the contrary, *in vivo*, the increase in tumor oxygenation (induced by carbogen challenge) led to a similar metabolic shift in glucose metabolism in both tumor models. The major discordance in metabolic patterns observed *in vitro* and *in vivo* highlights that any extrapolation of *in vitro* metabolic profiling to the *in vivo* situation should be taken cautiously and that metabolic phenotyping using molecular imaging is mandatory *in vivo*.

*Neoplasia (2016) 18, 742–752*

## Introduction

Enhanced glycolysis has for a long time been recognized as a common metabolic feature of cancer [1–3]. Otto Warburg identified in the 1920s the presence of a faster glycolytic flux in tumor cells [4], characterized by a high glucose uptake and increased lactate production even in the presence of oxygen. Despite a limited capacity for ATP production, aerobic glycolysis confers a major advantage to tumor cells by supporting proliferation and biomass production [3,5,6]. During decades, the loss of coupling between

Address all correspondence to: Bernard Gallez, Biomedical Magnetic Resonance Unit–REMA, Louvain Drug Research Institute (LDRI), Université catholique de Louvain, Avenue Mounier, 73.08, B-1200 Brussels.
E-mail: bernard.gallez@uclouvain.be

[1]This study was funded by grants from the Belgian National Fund for Scientific Research (F.S.R.-FNRS; PDR T.0107.13), the Fonds Joseph Maisin, the Action de Recherches Concertées ARC 14/19-058, Belgian Science Policy Office Interuniversity Attraction Pole IUAP #P7/03, and intramural National Institute of Health funds.
Received 7 September 2016; Revised 25 October 2016; Accepted 27 October 2016


1476-5586
http://dx.doi.org/10.1016/j.neo.2016.10.010

glycolysis and oxidative phosphorylation (OXPHOS) in tumor cells has been assigned to major mitochondrial dysfunctions [7]. However, new evidence of oxidative activities in tumor cells has challenged this paradigm [8–12]. Indeed, some tumor cells majorly rely on OXPHOS for energy production, and besides the Warburg and oxidative phenotypes, some cancer exhibits hybrid phenotypes with an acquired metabolic flexibility.

Tumor metabolic alterations recently emerged as enticing targets for the development of anticancer treatments [13–16]. To identify potential treatment strategies, the specific descriptions of biochemical pathways and metabolic alterations are commonly carried out in well-established tumor models via *in vitro* phenotyping, which provides specific tests that can define distinct metabolic profiles. *In vivo* tumor models are then generally selected based on these *in vitro* characterizations and used for preclinical studies before clinical translation. Because *in vitro* models do not reflect the complex structure and the metabolic heterogeneity of tumors, numerous factors could potentially be underestimated when translating the models from *in vitro* to *in vivo*. Vascularization, cell density, metabolic competition, cooperation, and commensalism with host cells could indeed contribute to the metabolic pattern exhibited by tumor cells.

Because some reports highlighted the potential influence of tumor environment on metabolic profile of cancer cells [17,18], the objective of the present study was to investigate if tumor models differ in their metabolic phenotypes *in vitro* and *in vivo*. To answer this question, a global metabolic study was carried out *in vitro* and *in vivo* using prototypical tumor models. The MDA-MB-231 human breast cancer model and the SiHa human cervical cancer model were selected based on a previous *in vitro* study describing the cell lines as glycolytic and oxidative, respectively [19]. Glucose metabolism was analyzed under hypoxic and oxygenated conditions. According to a paradigm extensively applied *in vitro*, we hypothesized that when passing from hypoxia to a better oxygenated state, a Warburg phenotype should conserve a glycolytic behavior, whereas an oxidative phenotype should metabolically switch from glycolysis to OXPHOS (Pasteur effect). Advanced imaging techniques including positron emission tomography (PET), electron paramagnetic resonance (EPR) imaging, and $^{13}$C-hyperpolarizated magnetic resonance spectroscopy (MRS) were used to characterize the metabolic phenotype *in vivo*. Our results identified major discordances between metabolic profiles determined *in vitro* and *in vivo*, highlighting the limitations of direct extrapolation of *in vitro* findings to the *in vivo* situation.

## Material and Methods

### *Cell Culture*

MDA-MB-231 (human breast cancer) and SiHa (human cervix squamous cell carcinoma) cell lines (American Type Culture Collection) were routinely cultured in Dulbecco's modified Eagle's medium containing 4.5 g/l of glucose supplemented with 10% fetal bovine serum and 1% penicillin-streptomycin.

### *Metabolic Fluxes In Vitro*

Glucose utilization and lactate production were measured from supernatants of cultured cells under hypoxia or after reoxygenation. Cells were seeded in six-well plates and incubated until 70% to 80% confluence under hypoxic condition (1% $O_2$). Before the initiation of the experiment, the incubation medium was removed. Cells were quickly washed, and medium was changed to a low-glucose medium without glutamine. The cells were returned in the incubator under hypoxic condition. After 4 hours under hypoxia, supernatant of cultured cells was sampled. Cells were then returned in the incubator to remain under constant hypoxia for 24 hours or moved to aerobic condition (21% $O_2$) during 20 hours. At the end of the experiment, a final sampling of supernatant was performed for each condition, constant hypoxia or reoxygenation. The protocol is summarized in Figure 1. The supernatants collected were deproteinized. Glucose and lactate concentrations in samples were measured using specific enzymatic assays on a CMA600 microdialysis analyzer (CMA Microdialysis AB, Solna, Sweden).

### *Animal and Tumor Models*

Animal studies were undertaken in accordance with Belgian and the Université catholique de Louvain ethical committee regulations (agreements number UCL/2010/MD/001 and UCL/2014/MD/026). EPR imaging and hyperpolarized $^{13}$C-MRS experiments were carried out in compliance with the Guide for the Care and Use of Laboratory Animal Resources (National Research Council, 1996) and approved by the National Cancer Institute (NCI) Animal Care and Use Committee.

To establish subcutaneous tumor models, a total of $10^7$ MDA-MB-231 cells or $10^7$ SiHa cells, amplified *in vitro*, were collected by trypsinization, washed three times with Hanks balanced salt solution, and resuspended in 200 µl of a 1:1 mixture of Matrigel (BD Biosciences) and Hanks balanced salt solution. For EPR spectroscopy, PET/computed tomography (CT) imaging, and microdialysis experiments, the tumor cells were inoculated subcutaneously into the right hind thigh of nude female NMRI mice (Janvier Le Genest-Saint-Isle, France). For EPR imaging and hyperpolarized $^{13}$C-MRS experiments, the tumor cells were inoculated subcutaneously into the right hind thighs of athymic nude female mice supplied by Frederick Cancer Research Center (Animal Production, Frederick, MD). The mice were kept under standard housing and feeding conditions. A total of 29 MDA-MB-231 tumors and 26 SiHa tumors were scanned of this study. All the experiments were performed when tumors reached 7 mm in diameter.

### *Tumor Metabolic Fluxes*

To evaluate the effect of different oxic conditions on tumor metabolism, tumor-bearing mice were scanned twice for the breathing challenge, air versus carbogen breathing, with 1 day between each condition. The experimental design for *in vivo* experiments is presented in Figure 2. Animals were anesthetized by inhalation of isoflurane (Forene, Abbot, England) mixed with either air (21% oxygen) or carbogen (5% $CO_2$/95% oxygen), depending on the breathing condition tested, in a continuous flow (2 l/min). Animals were warmed (approximately 35°C) throughout the anesthesia period, and breathing rate was maintained at 80 ± 10 breaths per minute using 1.5% to 2% isoflurane.

### *EPR Spectroscopy*

*In vivo* tumor $pO_2$ was monitored by EPR spectroscopy using charcoal as the oxygen-sensitive probe [20,21]. EPR spectra were recorded using a 1.1-GHz EPR spectrometer (Magnettech, Berlin, Germany). According to calibration curves made by measuring the EPR line width as a function of the $pO_2$ [22], the EPR spectra line width was converted to $pO_2$. A charcoal suspension (100 mg/ml) was

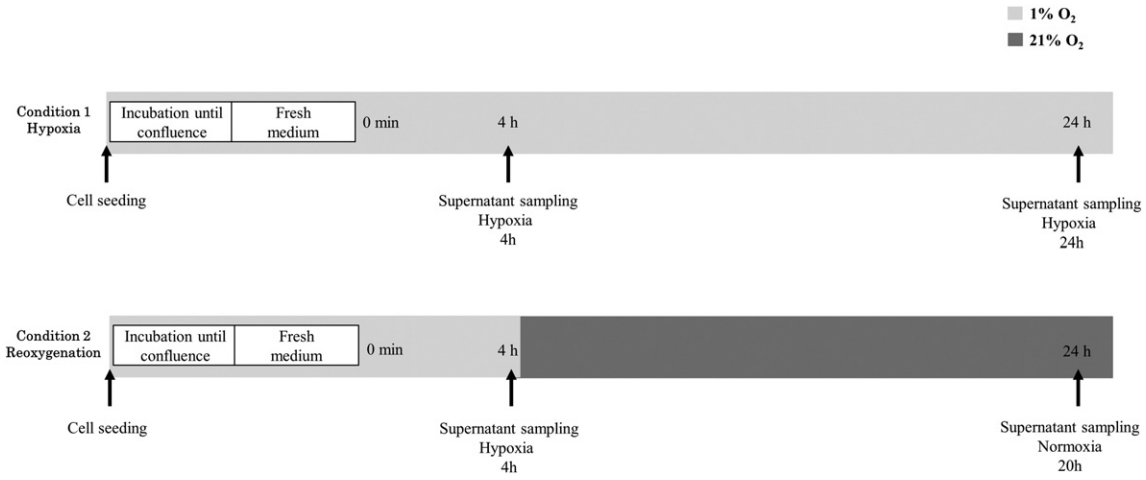


**Figure 1.** *In vitro* metabolic fluxes. The impact of different oxic conditions on tumor cell metabolism was investigated.

injected intratumorally (60 µl), and experiments were initiated 24 hours after EPR probe implantation [23]. For EPR readings, the tumor under study was placed in the center of the extended loop resonator whose sensitive volume extends 1 cm into the tumor mass. $pO_2$ measurements correspond to the average of $pO_2$ values in the tumor volume under study. For air condition, basal measurements were performed. For carbogen condition, $pO_2$ measurements were started after a 10-minute inhalation period. Crossed conditions were tested for the breathing challenge, the animal cohort was divided into two groups, and the following conditions were tested: day 1 air/day 2 carbogen or day 1 carbogen/day 2 air. The details of the protocol are presented in Figure 2*A*.

### *EPR Imaging*

Tumor $pO_2$ maps were obtained under air and carbogen breathing using an EPR imaging scanner equipped with a volume leg coil resonator tuned to 300 MHz. After the animal was positioned prone with the tumor-bearing leg placed inside the resonator, the EPR oxygen probe (OXO63, GE Healthcare) was injected intravenously as a 1.125-mmol/kg bolus through a cannula placed in the tail vein. EPR signals were obtained following the RF excitation pulses (60 nanoseconds, 80 W, 70° flip angle) using an analog-to-digital converter (200 megasamples/s). The repetition time was 8 microseconds. The free induction decay curves were collected under a nested loop of the *x*, *y*, and *z* gradients, and each time point in the free induction decay curve underwent phase modulation enabling three-dimensional (3D) spatial encoding. Anatomical reference was obtained using a 3-T magnetic resonance imaging (MRI) scanner (MR Solutions, Guildford, UK). The imaging protocol is detailed in Figure 2*B*. Co-registration of EPR and MRI images and data analysis were accomplished using MATLAB software (Mathworks). From the $pO_2$ images of the tumor, $pO_2$ frequency distributions and median tumor $pO_2$ were calculated.

### *PET/CT Imaging*

Tumor $^{18}$F-FDG uptake was assessed during the breathing challenge using PET/CT imaging. Whole-body PET imaging was performed on a dedicated small-animal PET scanner (Mosaic, Philips Medical Systems, Cleveland, OH) with a spatial resolution of 2.5 mm (full width at half maximum). The PET scans were followed by whole-body acquisitions using a helical CT scanner (NanoSPECT/CT Small Animal Imager, Bioscan Inc., Washington DC). For each breathing condition, anesthetized mice were injected 120 µl intraperitoneally with 11.1 to 14.8 MBq of $^{18}$F-FDG (Betaplus Pharma, Brussels, Belgium). A 10-minute transmission scan was first obtained in a single mode using a 370-MBq $^{137}$Cs source for attenuation correction. A 10-minute static PET acquisition was then performed after a 60-minute resting period. After the correction with attenuation factors obtained from the transmission scan, images were reconstructed using a fully 3D row action maximum likelihood algorithm in a 128 × 128 × 120 matrix, with a voxel size of 1 $mm^3$. After PET acquisition, anesthetized animals were transferred on the same bed from the PET scanner to the CT scanner (x-ray tube voltage: 55 kVp; number of projections: 180; exposure time 1000 milliseconds). The CT projections were reconstructed with a voxel size of 0.221 × 0.221 × 0.221 $mm^3$. The details of the imaging protocol are presented in Figure 2*A*. Regions of Interest (ROIs) were delineated on fused PET/CT images using PMOD software (PMOD, version 3.403, PMOD Technologies Ltd., Zurich, Switzerland). Two-dimensional ROIs were established on consecutive transversal slices using a 50% isocontour tool (ROI including the pixel values larger than 50% of the maximum pixel) that semiautomatically defined a 3D volume of interest (VOI) around the tissue of interest. To avoid overestimation of the uptake within the VOI, PET/CT fused images where used to discriminate hot pixels coming from the neighboring tissues like urinary bladder. Using the mean uptake within this VOI, the global tracer uptake was assessed in tumors and expressed as percentage of injected dose per gram of tissue (%ID/g). Crossed conditions were tested for the breathing challenge, the animal cohort was divided into two groups, and the following conditions were tested: day 1 air/day 2 carbogen or day 1 carbogen/day 2 air.

### *Microdialysis*

For the evaluation of tumor extracellular lactate content during the breathing challenge, we used microdialysis with a 6000-Da cutoff probe (Aurora Borealis) and a saline solution flux of 1 µl/min. Two probes were inserted per tumor under anesthesia 30 minutes before the collection of dialysates. Three baseline samplings were performed under air breathing. Then, the breathing gas was shifted to carbogen, and sampling was initiated after a 10-minute equilibration period

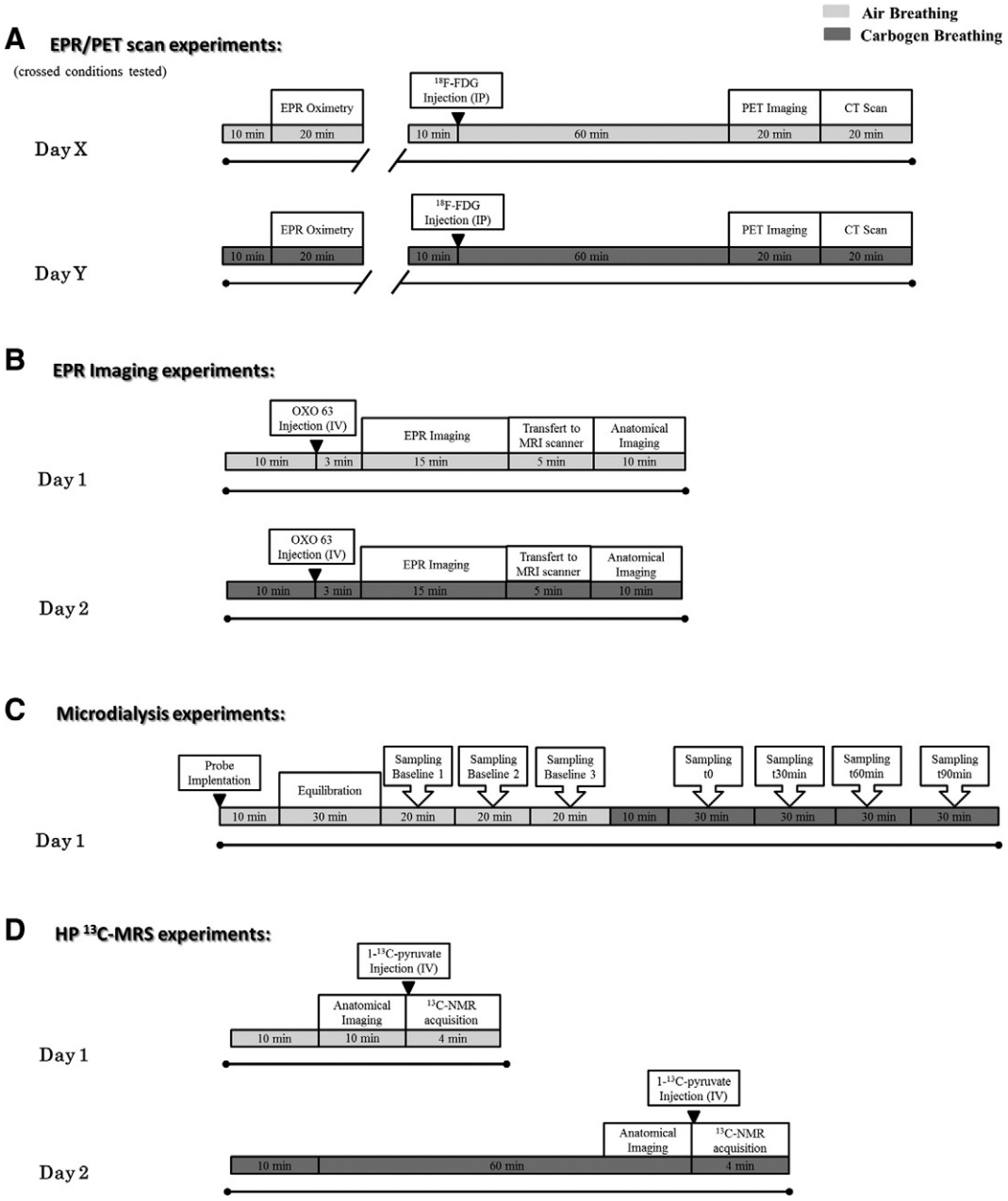


**Figure 2.** Experimental design built as a dynamic follow-up of the tumors during a breathing challenge. Tumor-bearing mice were scanned twice for the breathing challenge, air (light gray) versus carbogen (dark gray) breathing, with 1 day between each condition. Animals were anesthetized by inhalation of isoflurane mixed with either air (21% $O_2$) or carbogen (95% $O_2$/5% $CO_2$), depending on the breathing condition tested, in a continuous flow (2 l/min). Animals were warmed (approximately 35°C) throughout the anesthesia period. Anesthesia period is indicated by black lines. Breathing conditions are represented by light gray and dark gray shaded area for air and carbogen, respectively. (A) EPR spectroscopy and PET scan experiments. Crossed conditions were tested (conditions tested: day 1 air/day 2 carbogen or day 1 carbogen/day 2 air). (B) EPR imaging. (C) Microdialysis experiments. (D) Hyperpolarized $^{13}$C-MRS studies.

during 90 minutes. The lactate concentration in dialysates was determined using specific enzymatic assays on a CMA600 microdialysis analyzer (CMA Microdialysis AB, Solna, Sweden). The experimental design is displayed in Figure 2*C*.

### *Hyperpolarized $^{13}$C-MRS Studies*

1-$^{13}$C pyruvic acid (30 µl), containing 15 mM OXO63 and 2.5 mM gadolinium chelate ProHance (Bracco Diagnostics, Milano, Italy), was hyperpolarized at 3.35 T and 1.4 K using the Hypersense DNP polarizer (Oxford Instruments, Abingdon, UK) according to the manufacturer's instructions. After 60 to 90 minutes, the hyperpolarized sample was rapidly dissolved in 4.5 ml of a superheated alkaline buffer that consisted of 50 mM Tris(hydroxymethyl) aminomethane, 75 mM NaOH, and 100 mg/l of ethylenediaminetetraacetic acid. The hyperpolarized 1-$^{13}$C pyruvate solution (96 mM) was intravenously injected through a catheter placed in the tail vein of the mouse (12 µl/g body weight). Hyperpolarized $^{13}$C-MRS studies were performed on a 3-T scanner (MR Solutions, Guildford, UK). A home-built $^{13}$C solenoid leg coil 17.5 mm in diameter and 18.5 mm in length was used to closely

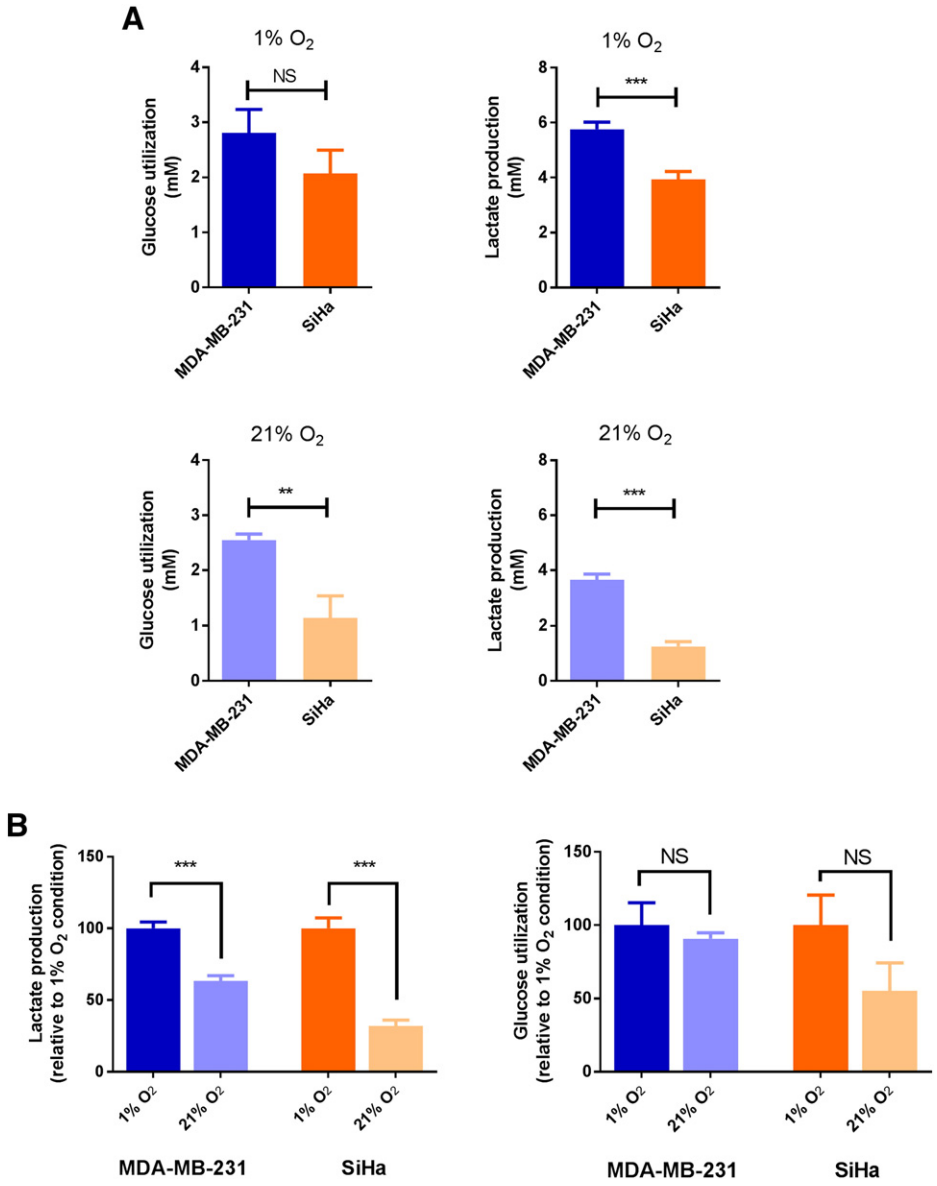


**Figure 3.** Metabolic behavior of MDA-MB-231 and SiHa cells under hypoxic and oxygenated conditions *in vitro*. (A) Under hypoxic condition (1% $O_2$), MDA-MB-231 cells produce high levels of lactate compared with SiHa cells. Under oxygenated condition (21% $O_2$), MDA-MB-231 cells maintained their glycolytic behavior. Data are expressed as means ± SEM. Unpaired tests were two-sided. (B) Effect of reoxygenation on lactate production and on glucose utilization in MDA-MB-231 cells and SiHa cells *in vitro*. SiHa cells are more sensitive to reoxygenation than MDA-MB-231 cells. Data are expressed as means ± SEM. Paired tests were two-sided.

conform to the size of the tumors upon measurement. After the rapid injection of hyperpolarized 1-$^{13}$C pyruvate, spectra were acquired every second for 240 seconds using a single pulse sequence. Data were analyzed in a model-free approach using the lactate/pyruvate ratio, calculated from the areas under the curves of the 1-$^{13}$C lactate peak and the 1-$^{13}$C pyruvate peak [24]. Additional details about the experimental design are presented in Figure 2*D*.

### *Statistical Analysis*

Analysis was performed using the GraphPad Prism 6 software. Results are expressed as means value of parameter ± SEM. All statistical tests were two-sided. Paired *t* test was used to compare mean changes between groups (air versus carbogen) for each tumor model, and unpaired *t* test was used to compare mean changes between the two tumor models. Results with $P < .05$ (*), <.01 (**), or <.001 (***) were considered to be statistically significant.

## Results

### *In Vitro, MDA-MB-231 Cells Exhibit a Glycolytic Behavior Even After Reoxygenation, Whereas SiHa Cells Are Oxidative Under Oxygenated Condition*

To assess the impact of different oxic conditions on tumor metabolism, we first evaluated the cellular metabolic fluxes under hypoxic and oxygenated conditions. Cells were kept during 4 hours under hypoxia (1% $O_2$) before undergoing reoxygenation (21% $O_2$) or remaining under constant hypoxia. Glucose utilization and lactate production were measured during the reoxygenation period or during the same period under hypoxia ($n = 3$ per model, triplicates) (Figure 3).

Under hypoxic condition (Figure 3*A*, 1% $O_2$), MDA-MB-231 cells produced high levels of lactate (5.76 ± 0.26 mM) compared with SiHa cells (3.93 ± 0.29 mM) ($P < .001$), but similar glucose consumption was measured in MDA-MB-231 cells (2.80 ± 0.43 mM) and SiHa cells

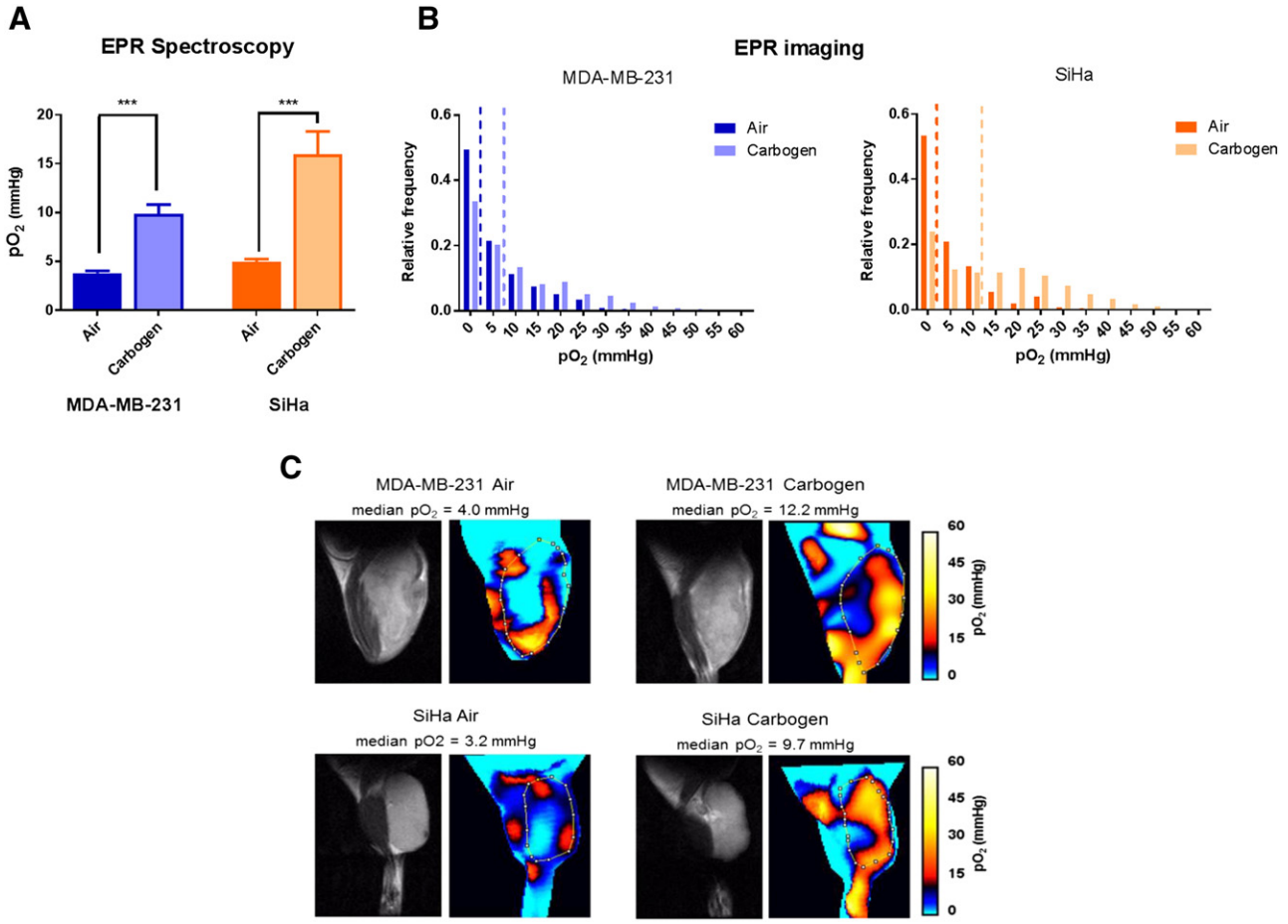


**Figure 4.** Effect of a breathing challenge on tumor oxygenation *in vivo*. These results show that hypoxic and oxygenated conditions are achieved under air and carbogen breathing, respectively, in MDA-MB-231 and SiHa tumors. (A) Changes of mean $pO_2$ under air and carbogen breathing measured by EPR spectroscopy. Data are expressed as means ± SEM. Paired tests were two-sided. (B) $pO_2$ frequency distributions in MDA-MB-231 and SiHa tumors as measured on EPR oxygen images. Lines indicated median $pO_2$ values for the collected data. (C) Representative EPR oxygen images of MDA-MB-231 and SiHa tumors obtained under air and carbogen breathing using EPR imaging. Region of interest was drawn on the tumor zone.

(2.07 ± 0.43 mM) ($P$ = .2416). Under oxygenated condition (Figure 3*A*, 21% $O_2$), glucose utilization was significantly different ($P$ = .0034) between for MDA-MB-231 cells (2.55 ± 0.11 mM) and SiHa cells (1.14 ± 0.39 mM). Also, MDA-MB-231 cells produced more lactate (3.65 ± 0.22 mM) than SiHa cells (1.25 ± 0.17 mM) ($P$ < .001).

To highlight a metabolic shift under different oxic conditions, we compared the metabolic fluxes of each cell line under hypoxic and oxygenated conditions (Figure 3*B*). By evaluating the variation of glucose utilization or lactate production under hypoxic and oxygenated conditions in each cell line, we noted that the reoxygenation majorly impacted SiHa compared with MDA-MB-231 cell metabolism. Indeed, for lactate production, MDA-MB-231 cells exhibit a decrease of 37% ($P$ < .001) compared with a decrease of 68% observed in SiHa cells ($P$ < .001). Glucose utilization was slightly but not significantly decreased by 9% in MDA-MB-231 cells ($P$ = .5710) and by 45% in SiHa cells ($P$ = .1300).

Even after reoxygenation, MDA-MB-231 cells remained more glycolytic than SiHa cells. Our results are consistent with previous phenotyping studies reporting MDA-MB-231 and SiHa cells as Warburg [19,25] and oxidative, respectively [19,26].

### *MDA-MB-231 and SiHa Tumors Are Hypoxic Under Air Breathing and Are Reoxygenated Under Carbogen Breathing*

To evaluate the metabolic behavior of these tumor cells *in vivo*, we designed experiments to study the global metabolism *in vivo* before and after reoxygenation induced by carbogen breathing. By changing $O_2$ availability in the tumor during the breathing challenge, we expected to achieve a hypoxic versus better oxygenated status in the models, thus mimicking the hypoxic versus oxygenated conditions tested *in vitro*.

In Figure 4, the effects of the breathing challenge on oxygenation were evaluated by EPR oximetry. Oxygenation increased after carbogen breathing in MDA-MB-231 ($n$ = 16, $P$ < .001) and in SiHa ($n$ = 12, $P$ < .001) tumors (Figure. 4*A*). Basal $pO_2$ values (air breathing) assessed by EPR spectroscopy were 3.8 ± 0.2 mm Hg for MDA-MB-231 tumors and 4.9 ± 0.3 mm Hg for SiHa tumors. Under carbogen breathing, MDA-MB-231 and SiHa tumors reached a $pO_2$ of 9.9 ± 0.95 mm Hg and 16.0 ± 2.3 mm Hg, respectively. These data were confirmed by EPR imaging measurements (MDA-MB-231: $n$ = 3; SiHa: $n$ = 5) (Figure 4, *B* and *C*). Typical $pO_2$ maps (Figure 4*C*) highlighted hypoxic tumors ($pO_2$< 10 mm Hg) under air breathing and a change of oxygenation after carbogen breathing. $pO_2$ frequency distributions were generated (Figure 4*B*)

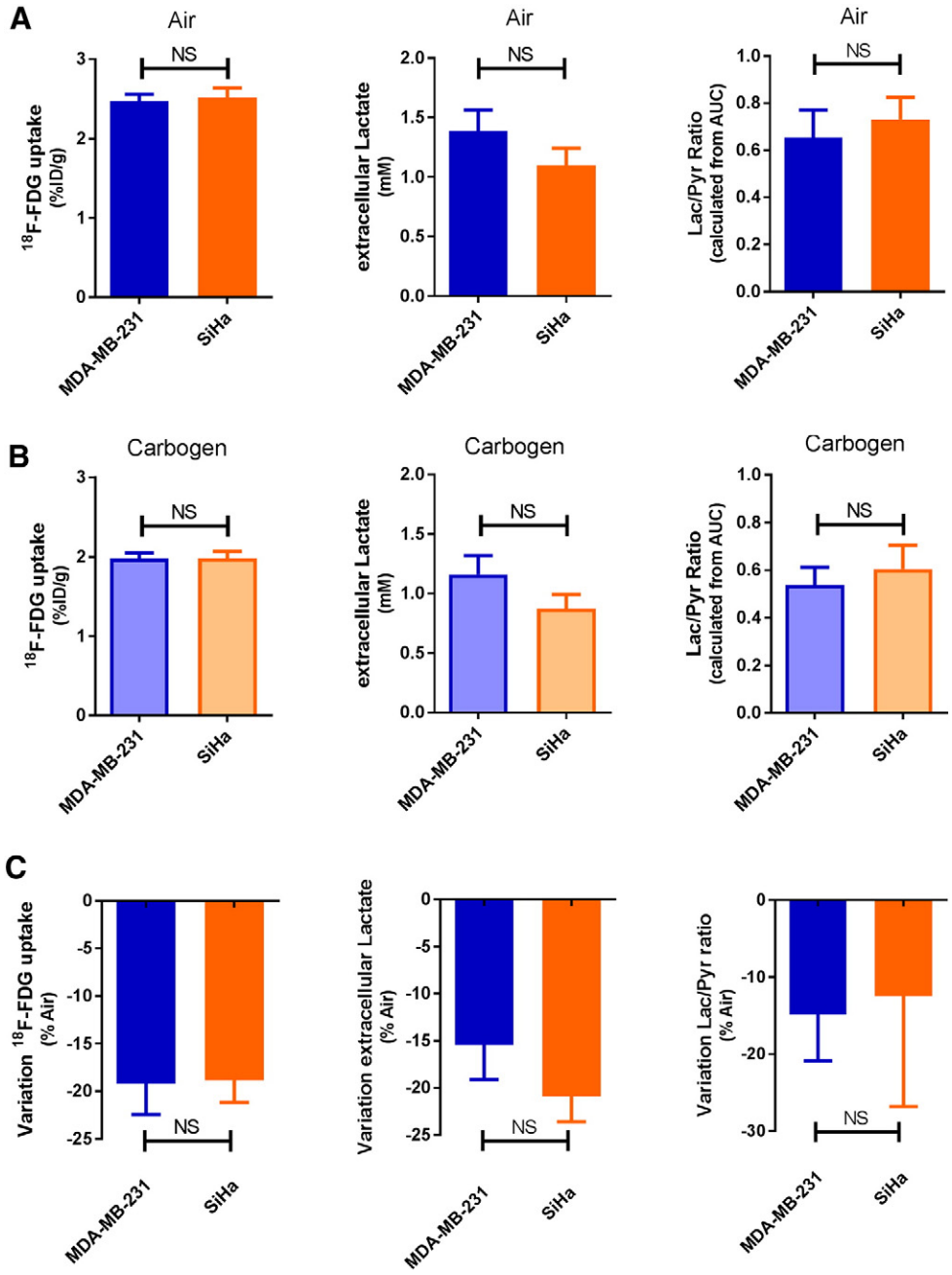


**Figure 5.** Metabolic behavior of MDA-MB-231 and SiHa tumors under air and carbogen breathing *in vivo*. The biomarkers tested were $^{18}$F-FDG uptake, extracellular lactate content during microdialysis experiments, and the transformation of pyruvate into lactate using hyperpolarized $^{13}$C-MRS. MDA-MB-231 and SiHa tumors exhibit the same phenotype under air (A) and also under carbogen (B) breathing. Data are expressed as means ± SEM. Unpaired tests were two-sided. The magnitude of response to the breathing challenge (variation) (C) is identical in both models. Data are expressed as means ± SEM. Unpaired tests were two-sided.

and highlighted the shift of median $pO_2$ induced by carbogen. Median $pO_2$ shifted from 2.6 to 6.5 mm Hg in MDA-MB-231 tumors and from 2.0 to 13.7 mm Hg in SiHa tumors.

These results demonstrate that hypoxic and oxygenated conditions are achieved under air and carbogen breathing, respectively, in both tumor models.

### *In Vivo, MDA-MB-231 and SiHa Tumors Exhibit the Same Phenotype Under Basal Condition and Under Carbogen Breathing*

To evaluate the metabolic behavior of the models *in vivo*, glucose uptake, extracellular lactate content, and lactate flux were measured in MDA-MB-231 and SiHa tumors under air (hypoxic condition) and carbogen (oxygenated condition) breathing (Figure 5).

Under air breathing, we observed a similar glycolytic behavior in MDA-MB-231 and in SiHa tumors, assessed by a high uptake of $^{18}$F-FDG, high lactate content (evaluated by microdialysis), and high lactate/pyruvate ratio (measured during hyperpolarized $^{13}$C-MRS studies) (Figure 5*A*). Under carbogen breathing, there was no appreciable difference in the metabolic profile of the two models (Figure 5*B*). However, a metabolic shift was observed after reoxygenation using carbogen in MDA-MB-231 and SiHa tumors. As presented in Figure 6, $^{18}$F-FDG uptake was significantly reduced in both models under carbogen (MDA: $n = 16$, $P < .001$; SiHa $n =$

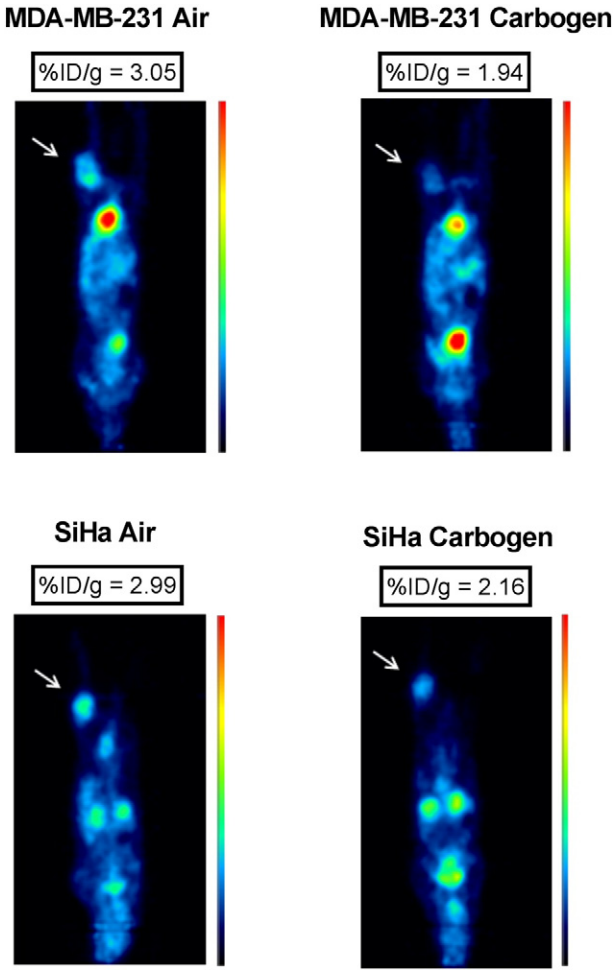


**Figure 6.** Representative $^{18}$F-FDG PET images showing MDA-MB-231 and SiHa tumor-bearing mice imaged under air and carbogen breathing. Tumors are indicated by thin arrows. $^{18}$F-FDG uptake is expressed in %ID/g. Images were normalized. $^{18}$F-FDG uptake drops after carbogen breathing in MDA-MB-231 and SiHa tumors.

12, $P < .001$). The extracellular lactate content in tumors significantly decreased under carbogen (MDA: $n = 4$, $P = .0162$; SiHa $n = 4$, $P = .0021$). This metabolic shift was also noted by measuring the conversion of pyruvate to lactate in the models (Figure 7) but did not reach a statistical significance (MDA: $n = 6$, $P = .0652$; SiHa $n = 5$, $P = .3913$). We also evaluated the magnitude of response to the breathing challenge by measuring the variation of these biomarkers between air and carbogen breathing conditions (Figure 5*C*). According to all the biomarkers tested, there was no difference in behavior between MDA-MB-231 and SiHa tumors during the breathing challenge ($P > .05$).

Together, the results obtained *in vivo* indicate that the MDA-MB-231 tumors do not appear more glycolytic than SiHa tumors, both models exhibiting the same metabolic behavior under the different conditions tested.

## Discussion

This study emphasizes a major limitation of describing the metabolic phenotype of tumors based on the *in vitro* studies solely. By evaluating glucose metabolism under different oxic conditions in two well-established glycolytic and oxidative tumor cell models, we challenged the Warburg and Pasteur effects, respectively. In the Warburg cellular model, in which metabolism is $O_2$-independent, we expected to preserve high rate of glycolysis even in the presence of oxygen, whereas in the oxidative cellular model, in which metabolism is sensitive to $O_2$, we expected to observe a switch from glycolysis to OXPHOS in the presence of a large amount of $O_2$ relative to baseline. This paradigm, extensively applied *in vitro*, has to our knowledge never been applied so far *in vivo*. By applying protocols with hypoxic and oxygenated conditions *in vitro* and *in vivo*, we identified a major difference in the metabolic behavior between both experimental conditions. *In vitro*, MDA-MB-231 cells kept their glycolytic metabolism even after reoxygenation (typical of a Warburg phenotype). On the contrary, SiHa cells shifted to an oxidative metabolism when oxygen became available, which is consistent with a Pasteur effect (Figure 3). The metabolic behavior was dramatically different *in vivo* for both tumor models: MDA-MB-231 tumors and SiHa tumors exhibited the same phenotype under hypoxia, and no difference was observed between both tumor models after reoxygenation induced by the carbogen breathing (Figure 5). These results highlight that the tumor microenvironment could be as important as the (epi)genetic profile to shape the tumor phenotype.

Our work extends recent efforts highlighting the limitation of *in vitro* studies to truly reflect the complex tumor behavior. Even if the microenvironment has already been presented as a decisive parameter determining the metabolic phenotype of tumors

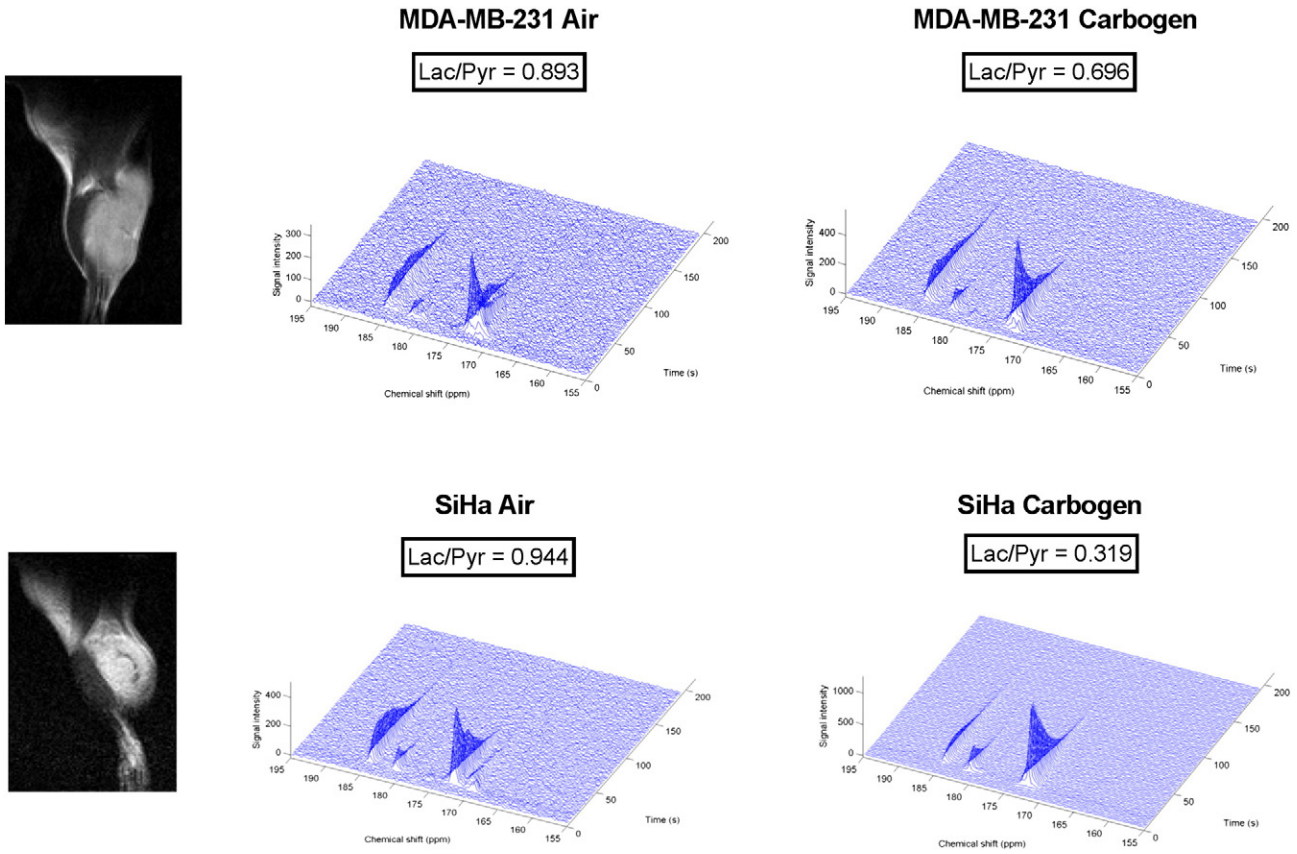


**Figure 7.** Typical $^{13}$C-MRS spectra from representative MDA-MB-231 tumors and SiHa tumors and corresponding $^{1}$H anatomical images. Lactate production, measured by the Lac/Pyr ratio, is reduced in MDA-MB-231 and SiHa tumors after carbogen breathing: pyruvate (173 ppm), lactate (185 ppm) peaks, and pyruvate hydrate (181 ppm).

[13,27,28], research has extensively focused on genetic and epigenetic alterations in cancer, and only a few studies have addressed the influence of the *in vivo* environment on the tumor metabolism. Davidson and colleagues recently investigated tissue metabolites from non–small cell lung tumors after the infusion of [U-$^{13}$C]glucose and [U-$^{13}$C]glutamine in mice [18]. Although lung cancer cells exhibited minor glucose oxidation *in vitro*, they established that glucose oxidation was required for tumor growth *in vivo*. Also, these authors identified a limited glutamine metabolism in lung tumor *in vivo* compared with lung cancer cells *in vitro* and suggested lactate as another preferred source of carbon in lung tumors. They also assessed that transplanted tumors exhibit a phenotype more similar to spontaneous lung tumors in mice compared with tumor cells in culture, highlighting the importance of model selection. In another recent study of Hensley and coworkers [17], metabolic activities related to perfusion were studied in human lung tumors based on multimodality imaging and $^{13}$C-glucose infusions. Poorly perfused areas, assessed by dynamic contrast-enhanced MRI, exhibited higher glucose metabolism compared with well perfused areas that preferentially relied on alternative fuels. Both these studies performed in lung cancer were able to identify common metabolic features in preclinical models and in patients, showing minimal resemblance with *in vitro* characterization.

Our present work adds to these studies in several ways. First, we showed that tumor cell models exhibit distinct metabolic behaviors *in vitro* but present the same behavior *in vivo* as attested by a multimodality imaging study. Although we reproduced similar experimental conditions *in vitro* and *in vivo*, we assessed that the paradigm, extensively applied *in vitro*, did not recapitulate the *in vivo* behavior of these models. The results observed *in vivo* could not be attributed to the impact of anesthesia on tumor hemodynamics as it was demonstrated previously that isoflurane had negligible effect on both tumor perfusion and oxygenation [29]. Also, the measurement repeatability was demonstrated during EPR spectroscopy and PET scan experiments. Indeed, crossed conditions were tested for the breathing challenge, and no difference was observed between the two subgroups in the animal cohort. Second, we assessed the occurrence of a rapid metabolic adaptation after carbogen breathing *in vivo* in both models. Carbogen breathing had a significant impact on $^{18}$F-FDG uptake and lactate content (Figure 5). This demonstrates the rapid plasticity of tumor cells to adapt their metabolism to the oxygen environment, a phenomenon known as the Pasteur effect. As already suggested by other studies [30,31], our data support that careful experimental protocol optimization is required for metabolic studies, likewise breathing conditions. However, regardless of the breathing gas used, the evaluation of tumor oxygenation in parallel to tumor metabolism studies would undoubtedly improve tumor phenotyping research. Third, the advanced imaging technologies used in the present study represent relevant tools for tumor metabolic phenotyping *in vivo*. $^{18}$F-FDG PET scan is a widespread technology already used in clinical routine, and hyperpolarized $^{13}$C-MRI is an emerging technology that was recently introduced in clinical research [32]. Our data suggest that molecular imaging techniques could

represent a powerful tool to identify metabolic alterations in patients and may be used as relevant biomarkers to guide treatments targeting tumor metabolism.

However, our study presents some limitations that should be addressed. First, host cells and tumor microenvironment could be involved in the divergence of metabolic metabolism between *in vitro* and *in vivo* studies. In our study, the metabolic profile was established *in vivo* considering results on the whole tumor. Using a global measurement of the tumor mass, we were not able to discriminate between host cell metabolism and cancer cell metabolism. Further investigations using co-culture models under different culture conditions should be considered to determine the role of host cell in metabolic profile measurements as well as the impact of nutrient availability, oxygenation, and acidification on tumor metabolism. Second, xenografts using immortalized cell lines represent the majority of the tumor models investigated due to their easy use. Nevertheless, this approach does not always correlate with clinical outcomes in patients, as the generation of cancer cell lines could majorly alter biologic and genetic properties and cause the loss of specific cell population. Third, the use of immunodeficient animals provides a less realistic tumor microenvironment. Therefore, it would be important to further explore primary cell cultures implanted in immunocompetent animals. Finally, comparative study involving different implantations such as subcutaneous or orthotopic should be considered.

In conclusion, our metabolic study identified distinct metabolic behaviors of two well-established tumor models *in vitro* and *in vivo*. Results suggest that there is a need to take cautiously any extrapolation of *in vitro* characterization to the *in vivo* situation. Implanted tumors and spontaneous cancer models should be preferred to identify relevant metabolic alterations within the milieu of the tumor microenvironment. When well-established tumor cell models are translated *in vivo*, additional phenotyping should be considered and could be achieved by using clinically relevant biomarkers like $^{18}$F-FDG PET scan and hyperpolarized $^{13}$C-MRI.

## Conflict of Interest

The authors disclose no potential conflicts of interest.

## Acknowledgements

This study was funded by grants from the Belgian National Fund for Scientific Research (F.S.R.-FNRS; PDR T.0107.13), the Fonds Joseph Maisin, the Action de Recherches Concertées ARC 14/19-058, Belgian Science Policy Office Interuniversity Attraction Pole IUAP #P7/03, and intramural National Institute of Health funds. M. A. N. is a Research Fellow and P. E. P. a Senior Postdoctoral Fellow of F.R.S.-FNRS. P. S. and B. F. J. are Research Associates of F.R.S.-FNRS.

## References

[1] López-Lázaro M (2008). The Warburg effect: why and how do cancer cells activate glycolysis in the presence of oxygen? *Anticancer Agents Med Chem* **8**(3), 305–312. http://dx.doi.org/10.2174/187152008783961932.

[2] Upadhyay M, Samal J, Kandpal M, Singh OV, and Vivekanandan P (2013). The Warburg effect: insights from the past decade. *Pharmacol Ther* **137**(3), 318–330. http://dx.doi.org/10.1016/j.pharmthera.2012.11.003.

[3] Vander Heiden MG, Cantley LC, and Thompson CB (2009). Understanding the Warburg effect: the metabolic requirements of cell proliferation. *Science* **324**(5930), 1029–1033. http://dx.doi.org/10.1126/science.1160809.

[4] Warburg O (1925). Uber den Stoffwechsel der Carcinomzelle. *Klin Wochenschr* **4**, 534–536. http://dx.doi.org/10.1007/BF01726151.

[5] Lunt SY and Vander Heiden MG (2011). Aerobic glycolysis: meeting the metabolic requirements of cell proliferation. *Annu Rev Cell Dev Biol* **27**, 441–464. http://dx.doi.org/10.1146/annurev-cellbio-092910-154237.

[6] De Preter G, Neveu MA, Danhier P, Brisson L, Payen VL, and Porporato PE, et al (2016). Inhibition of the pentose phosphate pathway by dichloroacetate unravels a missing link between aerobic glycolysis and cancer cell proliferation. *Oncotarget* **7**(3), 2910–2920. http://dx.doi.org/10.18632/oncotarget.6272.

[7] Warburg O (1956). On respiratory impairment in cancer cells. *Science* **124**(3215), 269–270. http://dx.doi.org/10.1126/science.124.3215.267.

[8] Moreno-Sanchez R, Rodriguez-Enriquez S, Marin-Hernandez A, and Saavedra E (2007). Energy metabolism in tumor cells. *FEBS J* **274**(6), 1393–1418. http://dx.doi.org/10.1111/j.1742-4658.2007.05686.x.

[9] Moreno-Sanchez R, Marin-Hernandez A, Saavedra E, Pardo JP, Ralph SJ, and Rodriguez-Enriquez S (2014). Who controls the ATP supply in cancer cells? Biochemistry lessons to understand cancer energy metabolism. *Int J Biochem Cell Biol* **50**, 10–23. http://dx.doi.org/10.1016/j.biocel.2014.01.025.

[10] Xie J, Wu H, Dai C, Pan Q, Ding Z, and Hu D, et al (2014). Beyond Warburg effect—dual metabolic nature of cancer cells. *Sci Rep* **4**, 4927. http://dx.doi.org/10.1038/srep04927.

[11] Obre E and Rossignol R (2015). Emerging concepts in bioenergetics and cancer research: metabolic flexibility, coupling, symbiosis, switch, oxidative tumors, metabolic remodeling, signaling and bioenergetic therapy. *Int J Biochem Cell Biol* **59**, 167–181. http://dx.doi.org/10.1016/j.biocel.2014.12.008.

[12] Jose C, Bellance N, and Rossignol R (2011). Choosing between glycolysis and oxidative phosphorylation: a tumor's dilemma? *Biochim Biophys Acta* **1807**(6), 552–561. http://dx.doi.org/10.1016/j.bbabio.2010.10.012.

[13] Hanahan D and Weinberg RA (2011). Hallmarks of cancer: the next generation. *Cell* **144**(5), 646–674. http://dx.doi.org/10.1016/j.cell.2011.02.013.

[14] Porporato PE, Dhup S, Dadhich RK, Copetti T, and Sonveaux P (2011). Anticancer targets in the glycolytic metabolism of tumors: a comprehensive review. *Front Pharmacol* **2**, 49. http://dx.doi.org/10.3389/fphar.2011.00049.

[15] Tennant DA, Duran RV, and Gottlieb E (2010). Targeting metabolic transformation for cancer therapy. *Nat Rev Cancer* **10**(4), 267–277. http://dx.doi.org/10.1038/nrc2817.

[16] Bost F, Decoux-Poullot AG, Tanti JF, and Clavel S (2016). Energy disruptors: rising stars in anticancer therapy? *Oncogenesis* **5**, e188. http://dx.doi.org/10.1038/oncsis.2015.46.

[17] Hensley CT, Faubert B, Yuan Q, Lev-Cohain N, Jin E, and Kim J, et al (2016). Metabolic heterogeneity in human lung tumors. *Cell* **164**(4), 681–694. http://dx.doi.org/10.1016/j.cell.2015.12.034.

[18] Davidson SM, Papagiannakopoulos T, Olenchock BA, Heyman JE, Keibler MA, and Luengo A, et al (2016). Environment impacts the metabolic dependencies of Ras-driven non–small cell lung cancer. *Cell Metab* **23**(3), 517–528. http://dx.doi.org/10.1016/j.cmet.2016.01.007.

[19] De Preter G, Danhier P, Porporato PE, Payen VL, Jordan BF, and Sonveaux P, et al (2016). Direct evidence of the link between energetic metabolism and proliferation capacity of cancer cells in vitro. *Adv Exp Med Biol* **876**, 209–214. http://dx.doi.org/10.1007/978-1-4939-3023-4_26.

[20] Gallez B, Jordan BF, Baudelet C, and Misson PD (1999). Pharmacological modifications of the partial pressure of oxygen in murine tumors: evaluation using in vivo EPR oximetry. *Magn Reson Med* **42**(4), 627–630.

[21] Jordan BF, Baudelet C, and Gallez B (1998). Carbon-centered radicals as oxygen sensors for in vivo electron paramagnetic resonance: screening for an optimal probe among commercially available charcoals. *MAGMA* **7**(2), 121–129.

[22] Gallez B, Baudelet C, and Jordan BF (2004). Assessment of tumor oxygenation by electron paramagnetic resonance: principles and applications. *NMR Biomed* **17**(5), 240–262. http://dx.doi.org/10.1002/nbm.900.

[23] Charlier N, Beghein N, and Gallez B (2004). Development and evaluation of biocompatible inks for the local measurement of oxygen using in vivo EPR. *NMR Biomed* **17**(5), 303–310. http://dx.doi.org/10.1002/nbm.902.

[24] Hill DK, Orton MR, Mariotti E, Boult JK, Panek R, and Jafar M, et al (2013). Model free approach to kinetic analysis of real-time hyperpolarized 13C magnetic resonance spectroscopy data. *PLoS One* **8**, e71996. http://dx.doi.org/10.1371/journal.pone.0071996.

[25] Gatenby RA and Gillies RJ (2004). Why do cancers have high aerobic glycolysis? *Nat Rev Cancer* **4**(11), 891–899. http://dx.doi.org/10.1038/nrc1478.

[26] Sonveaux P, Vegran F, Schroeder T, Wergin MC, Verrax J, and Rabbani ZN, et al (2008). Targeting lactate-fueled respiration selectively kills hypoxic tumor cells in mice. *J Clin Invest* **118**(12), 3930–3942. http://dx.doi.org/10.1172/JCI36843.

[27] Cairns RA, Harris IS, and Mak TW (2011). Regulation of cancer cell metabolism. *Nat Rev Cancer* **11**(2), 85–95. http://dx.doi.org/10.1038/nrc2981.

[28] Davidson SM and Vander Heiden MG (2012). METabolic adaptations in the tumor MYCroenvironment. *Cell Metab* **15**(2), 131–133. http://dx.doi.org/10.1016/j.cmet.2012.01.005.

[29] Baudelet C and Gallez B (2004). Effect of anesthesia on the signal intensity in tumors using BOLD-MRI: comparison with flow measurements by laser Doppler flowmetry and oxygen measurements by luminescence-based probes. *Magn Reson Imaging* **22**(7), 905–912. http://dx.doi.org/10.1016/j.mri.2004.02.005.

[30] Fueger BJ, Czernin J, Hildebrandt I, Tran C, Halpern BS, and Stout D, et al (2006). Impact of animal handling on the results of 18F-FDG PET studies in mice. *J Nucl Med* **47**, 999–1006.

[31] Stout D, Berr SS, LeBlanc A, Kalen JD, Osborne D, and Price J, et al (2013). Guidance for methods descriptions used in preclinical imaging papers. *Mol Imaging* **12**, 1–15. http://dx.doi.org/10.2310/7290.2013.00055.

[32] Nelson SJ, Kurhanewicz J, Vigneron DB, Larson PE, Harzstark AL, and Ferrone M, et al (2013). Metabolic imaging of patients with prostate cancer using hyperpolarized [1-(1)(3)C]pyruvate. *Sci Transl Med* **5**(198), 198ra08. http://dx.doi.org/10.1126/scitranslmed.3006070.